PHYSICAL REVIEW C VOLUME 45, NUMBER 5 MAY 1992

Electromagnetic dissociation of relativistic ^{28}Si into $p+^{27}$Al

J. Barrette,[4] R. Bellwied,[7],[a] P. Braun-Munzinger,[7] W. E. Cleland,[6] G. David,[7] J. Dee,[7] O. Dietzsch,[8] E. Duek,[1],[b] M. Fatyga,[1] D. Fox,[3],[c] S. V. Greene,[10] J. R. Hall,[5] T. K. Hemmick,[10],[d] N. Herrmann,[7],[e] R. W. Hogue,[1] B. Hong,[7] K. Jayananda,[6],[f] D. Kraus,[6] B. Shiva Kumar,[10] R. Lacasse,[4] D. Lissauer,[1] W. J. Llope,[7] T. Ludlam,[1] R. Majka,[10] D. Makowiecki,[1] S. K. Mark,[4] S. McCorkle,[1] J. T. Mitchell,[10] M. Muthuswamy,[7] E. O'Brien,[1] V. Polychronakos,[1] C. Pruneau,[4] F. S. Rotondo,[10] J. Sandweiss,[10] J. Simon-Gillo,[9],[g] U. Sonnadara,[6] J. Stachel,[7] H. Takai,[1] E. M. Takagui,[6],[h] T. G. Throwe,[1] L. Waters,[7],[g] W. J. Willis,[2] C. Winter,[10] K. Wolf,[9] D. Wolfe,[5] C. L. Woody,[1] N. Xu,[7] Y. Zhang,[7] Z. Zhang,[6] and Z. Zou[7]

(E814 Collaboration)

[1] *Brookhaven National Laboratory, Upton, New York 11973*
[2] *European Organization for Nuclear Research (CERN), Geneva, Switzerland*
[3] *Los Alamos National Laboratory, Los Alamos, New Mexico 87545*
[4] *McGill University, Montreal, Québec, Canada*
[5] *University of New Mexico, Albuquerque, New Mexico 87131*
[6] *University of Pittsburgh, Pittsburgh, Pennsylvania 15260*
[7] *State University of New York, Stony Brook, New York 11794*
[8] *Universidade de São Paulo, São Paulo, Brazil*
[9] *Texas A&M University, College Station, Texas 77843*
[10] *Yale University, New Haven, Connecticut 06511*

(Received 13 December 1991)

We report a direct measurement of the final-state energy spectrum in the electromagnetic dissociation of ^{28}Si into $p+^{27}$Al at an energy of 14.6 GeV/nucleon. The final-state energy is obtained through a calculation of the p-^{27}Al invariant mass in kinematically reconstructed events. The final-state energy spectrum for all targets is peaked near the isovector giant-dipole resonance in ^{28}Si and the dependence of the magnitude of the cross section on target charge confirms that the excitation is largely electromagnetic. By exploiting the expected scaling behavior on target Z and A, the background from nuclear interactions is evaluated and subtracted, leaving a pure electromagnetic dissociation final-state energy distribution. This distribution is well reproduced by simulated events, in which the photon spectrum calculated in the Weizsäcker-Williams approximation is combined with experimental data on the photonuclear reaction ^{28}Si$(\gamma,p)^{27}$Al, and slight differences are observed only at low final-state energy.

PACS number(s): 25.75.+r

I. INTRODUCTION

The electromagnetic excitation of nuclei in peripheral heavy ion collisions can be very important at high energies, due to the relativistic enhancement of the Coulomb field of the target, as seen in the rest frame of the projectile. This can lead to very large cross sections for the electromagnetic dissociation (EMD) of relativistic heavy ion projectiles. Such EMD has been observed in a number of experiments at a variety of beam energies [1–5]. The main evidence that the process is electromagnetic in nature arises from the observation that the cross sections exhibit an approximate Z^2 dependence, which is naively expected for an electromagnetic process. The excitation

[a] Present address: Dept. of Physics, Wayne State University, Detroit, MI 48202.
[b] Present address: SSC Laboratory, MS 1070, 2550 Beckleymeade Ave, Dallas, TX 75248.
[c] Present address: Indiana University Cyclotron Facility, 2401, Bloomington, IN 47405.
[d] Present address: Dept. of Physics, State University of New York, Stony Brook, NY 11794.
[e] Present address: Physikalisches Institut, Universität Heidelberg, D 69 Heidelberg, Germany.
[f] Present address: Dept. of Physics, University of Sri Jayewardenepura, Nugegoda, Sri Lanka.
[g] Present address: Los Alamos National Laboratory, Los Alamos, NM 87545.
[h] On leave of absence from Universidade de São Paulo, São Paulo, Brazil.

can be viewed at relativistic energies as an absorption of one or more virtual photons. The flux of the virtual photons can be calculated using the Weizsäcker-Williams (WW) method [6, 7]. A detailed study of this process that would include a measurement of the excitation energy distribution would be a much more severe test of our understanding of the electromagnetic excitation mechanism at relativistic energies.

In a previous work [1] we measured the cross sections for the EMD of ^{28}Si into final states containing one, two, or three nucleons. The one-nucleon removal cross sections were found to agree with that expected from a folding of the WW photon spectrum produced by the target with the dipole strength function of the projectile. Similar conclusions have been reached by Brechtmann *at al.* [9] and Llope and Braun-Munzinger [10].

In this paper we report the results of a much more detailed study of the EMD of ^{28}Si into p+^{27}Al, presenting the first measurements of the final-state energy spectrum and decay angular distributions for this process. The final-state energy is defined as the invariant mass of the p-^{27}Al system less the ^{28}Si rest mass. It is equal to the difference between the excitation energy of the ^{28}Si and that of the ^{27}Al. Thus the final-state energy is equal to the excitation energy in events in which the decay proceeds to the ground state of ^{27}Al. The experiment (BNL E814) was done at the Alternating Gradient Synchrotron (AGS) at Brookhaven National Laboratory using a ^{28}Si beam at 14.6 GeV/nucleon, incident on targets of Pb, Sn, Cu, Al, and C. In the following we describe the experimental setup used, the selection criteria utilized to extract the proton emission via EMD, and the process of kinematic reconstruction. We give new results for the integrated cross section for this process, which confirm our previous measurement, and compare our results for the final-state energy spectrum with that expected in a virtual photon model.

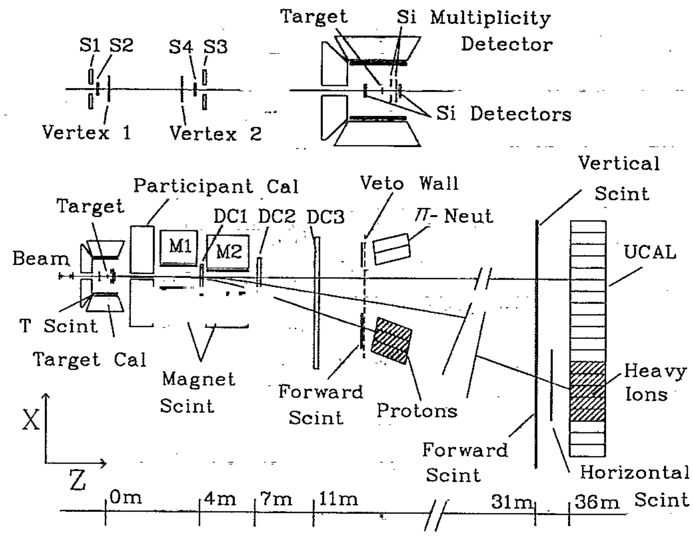

FIG. 1. Diagram of the E814 apparatus. The beam enters through a hole in the back wall of the target calorimeter. Forward-going particles pass through the participant calorimeter opening, and the magnets M1 and M2, which provide the deflection for the forward spectrometer. Track positions are measured in drift chambers DC1, DC2, and DC3. Charge is measured in the forward scintillators and energy is measured in the U/Cu calorimeters.

II. EXPERIMENTAL SETUP

The apparatus used in experiment E814 is shown in Fig. 1. It is identical to the setup used in the previous experiment with the addition of several new detectors and an improved trigger system. A description of the detectors used in previous experiments is given in Ref. [1], along with a description of the specific functions they perform. A brief description of these detectors and a more complete description of the new detectors is given below. The coordinate system used in this experiment is defined by a right-handed system with z along the incident beam direction and y vertical (upward).

The original complement of detectors consisted of a beam telescope, a set of detectors in the target area to aid in the distinction between EMD and nuclear interactions through the detection of target or projectile fragments, and a set of detectors in the forward spectrometer for identifying the final-state particles and measuring their energy. The tracking detectors and participant calorimeter had been installed but were not used for the previous measurement.

The *beam telescope* consists of a set of four scintillation counters, two of which are veto counters with holes, through which the beam of 6 mm diameter passes. The detectors used for vetoing events arising from nuclear interactions consist of the *target calorimeter*, an array of 992 NaI crystals; the *target scintillators*, a set of 52 scintillators lining the inside face of the target calorimeter; the *multiplicity detector*, two silicon pad detectors divided into 512 elements each; and the *magnet scintillators*, a set of 16 counters placed on the lateral walls of the two spectrometer magnets. The detectors in the spectrometer consist of *U/Cu-scintillator calorimeters* (UCAL) for energy and position measurement, and *forward scintillators* mounted immediately upstream of them for charge (Z), vertical position, and time of flight measurements. The downstream detectors were placed at two z-locations. At $z = 12$ m, the $|Z/A| = 1$ particles were detected in either the proton region, consisting of three calorimeters and six scintillators, or the π^0 region, consisting of two calorimeters and four scintillators. At $z = 36$ m, particles with either $Z/A = 0$ or $|Z/A| < 1$ were detected in an array of 20 calorimeters and 39 scintillators.

For the present experiment, the following additional detectors were employed both to reduce the background level and to permit kinematic reconstruction.

(i) Beam vertex detector.—Two silicon strip detectors of thickness 300 μm were placed in the incident beam line to define the horizontal angle and position of the incident beam. The vertical strips had a pitch of 50 μm, and the two planes were separated by 3.0 m, giving an angular resolution of better than 15 μsr. The hit pattern in these detectors is recorded for each event.

(ii) Upstream and downstream Si detectors.—A set of two surface barrier silicon detectors 1.0 cm in diameter and 100 μm thick were used to identify the charge of the incoming and outgoing particles. These detectors were positioned as close as possible to the target, one on the upstream side and the other on the downstream side.

(iii) Participant calorimeter.—A lead-scintillator calorimeter read out through wavelength shifting fibers into 512 photomultiplier tubes is used to improve our veto against nuclear interactions.

(iv) Horizontal counters.—A scintillation counter array consisting of five horizontal counters of dimensions $10\times1\times120$ cm^3 was placed downstream of the vertical scintillator array and centered on the distribution of deflected beam particles. These counters are used to provide additional information on the charge measurement of the heavy ion fragments.

(v) Veto wall.—An additional set of scintillation counters, placed above and below the beam line in a vertical plane at $z = 12$ m. These counters are mounted sufficiently far from the horizontal plane to be in the shadow of the forward collimation system and are used to veto background events caused by interactions downstream of the magnets.

(vi) Drift chambers.—The tracking chambers used in this experiment consist of one chamber DC1, located between the two magnets, with one plane of cathode pad readout, and two composite chambers DC2 and DC3, located 6.9 and 11.6 m downstream of the target, respectively. These two chambers are of identical design except for size and number of wires. They consist of six planes of drift wires, which are used to establish the horizontal track coordinates, and one plane of wires read out by chevron-shaped segmented cathode pads, which are used to determine the vertical coordinate by interpolating between readouts spaced 3.0 to 10.0 cm apart, depending on their position in the plane. The spacing of the sense wires for both sections is 6.35 mm in DC2 and 12.70 mm in DC3. The location of the drift wires in the drift section is staggered by one-half of their separation in alternate planes, a feature exploited in the track recognition to eliminate uncorrelated hits and hits due to δ electrons. A more detailed description of these chambers and measurements of their resolution for minimum ionizing particles is given elsewhere [11, 12].

The trigger for the set of data analyzed here was similar to that used in our previous work. We required a coincidence between protons as detected by the proton calorimeters and a heavy fragment with charge near that of the projectile as measured in the downstream Si detector and the forward scintillators in the region of the beam. In order to reduce the background from downstream interactions, in which a $Z = 14$ beam particle leaves the target, we required in the trigger that the charge seen by the downstream Si detector be $Z = 13$ or less. In the forward scintillator system, we also required that a charged particle of at least $Z = 8$ be present. For this measurement an on-line veto on the basis of detectors surrounding the target was implemented, thus enhancing the sample of EMD events.

The E814 trigger system is designed to allow data taking with parallel triggers, with the possibility to downscale (i.e., accept only a fraction of) triggers in any channel. During this run, we simultaneously took data with $1p$ and $1n$ in the final state. In addition, we added a number of partial triggers for use in the analysis, all of which were downscaled appropriately. These included $1p$ and $1n$ triggers without the veto condition, triggers with only the proton calorimeter requirement (pretriggers), and beam triggers. In addition, random events, in which a beam requirement was not made, were taken in order to correct for pedestal variations and to study other systematic effects. For every trigger, signals from all detectors were digitized and recorded on magnetic tape for offline analysis.

Data were taken with natural targets of Pb, Sn, Cu, Al, and C, each with a thickness of 0.04 nuclear interaction length. The physical thicknesses were 4.36, 3.25, 2.24, 1.30, and 0.60 g/cm^2, respectively. In addition, data were taken with an empty target holder to evaluate interactions originating from materials other than the target. The data sample consists of a total of approximately 80 000 $1p$ triggers, of which 17 495 were selected for cross-section evaluation, as discussed below.

III. DATA ANALYSIS

The EMD is a very low momentum transfer collision, compared to one induced by strong interactions. However, low momentum transfer or "soft" nuclear collisions can produce the same final state, and these events are the major background for EMD events. In the off-line data reduction, criteria are applied to select events which produce very little activity in the target region.

The upstream detector group described in Sec. II was used with the following cuts, in order to identify reaction products originating from pure electromagnetic collisions.

(i) Beam telescope and upstream Si detector.—Pulse height cuts are imposed to select good beam particles. Events in which two beam particles are closer than 2.5 μs in time or in which the beam particle interacted upstream of the target are rejected.

(ii) Target scintillators.—A loose cut is made on hit multiplicity in these counters since they are sensitive not only to nuclear fragments but also to δ electrons emitted when a heavy ion traverses the target. Events with multiplicity above 4 are rejected.

(iii) Target calorimeter.—The NaI calorimeter is useful in rejecting collisions in which the target is fragmented. We remove events in which any of the NaI signals contain more than 20 MeV, well above the noise level of 2 MeV rms.

(iv) Multiplicity detector.—The silicon pad detector is sensitive to projectile fragments which are emitted in the forward direction, and to δ rays. With events triggered only on the beam coincidence, the typical multiplicity is 10 hits. Events with 25 or more hits are rejected in this analysis.

(v) Participant calorimeter.—Because of its large solid angle coverage in the forward direction ($0.8 < \eta < 4.2$), its insensitivity to δ electrons, and its low noise of about σ

= 5 MeV, this detector is a powerful tool for the rejection of nuclear-induced fragmentation. We reject any event in which a deposit of above 200 MeV is seen in any of the cells (electromagnetic or hadronic) in the detector. In addition, a cut at 1.0 GeV for total energy is applied to reject events in which the energy is spread over many cells.

(vi) Magnet scintillators.—These counters are sensitive to charged particles whose magnetic rigidity is significantly lower than that of the beam, since they are deflected to the side walls of the magnet. These counters have a photomultiplier tube at both ends of a long scintillator slab, and a cut based upon the number of photomultipliers with pulse height found above a low threshold is made. We reject events in which the multiplicity of such hits is 5 or greater.

In selecting $p+^{27}$Al events, we need to identify the heavy fragment with Z=13 and A=27. We use the downstream Si detector to measure the charge of the final-state products immediately after the target. The combination of the forward scintillators (vertical and horizontal) provide a measurement of the charge of the heavy fragment at the downstream end of the spectrometer. In Fig. 2 we show the measured pulse height spectrum of the heavy ions for $1p$ triggered events. Effects of scintillator saturation are removed in this plot, and the pulse heights have been plotted on a scale linear in Z^2 in which $Z = 14$ is at channel 1000. For $Z = 13$ particles we achieve a fractional resolution of 2.7%.

A rough Z/A value is estimated and used to verify the mass of the heavy fragment by combining the horizontal position extracted from the UCAL position algorithms and the position measured via pulse height ratios in the horizontal counters. This combination gives us a resolution of $\sigma \approx 2$ cm in the horizontal position of the heavy fragments, and we require that the position fall within the band of possible values for $Z/A = 13/27$. To suppress background from final states containing Al isotopes other than ^{27}Al, we reject events in which a cluster of energy 4 GeV or greater is found in the neutron calorimeters. We estimate that the contamination of ^{26}Al in our sample is about 1%. The cross-section ratio for the $p+n+^{26}$Al to $p+^{27}$Al channels is approximately 0.10 [1], and the probability for a neutron to escape detection is approximately 10%, leading to the above estimate. The background for ^{25}Al events is estimated to be about two orders of magnitude smaller because of the smaller production cross section and the presence of two neutrons in the final state. In addition, a set of requirements are imposed to identify the proton in the final state, using the proton calorimeters and the upstream forward scintillators. Clustering algorithms for the calorimeter data provide a resolution of $0.6/\sqrt{E}$, which is adequate to distinguish events with single protons from those with multiple protons in the final state.

TABLE I. Estimated efficiency for cross-section analysis. The efficiencies for the different selection criteria, assumed to be independent of one another, are values measured with pretrigger events, a data sample which is essentially unbiased by the trigger.

Selection criteria	Efficiency (%)
Downstream interactions	70.6 ± 1.9
Veto wall	87.5 ± 1.8
On-line veto detectors	76.9 ± 1.4
Good beam definition	84.3 ± 2.7
UCAL clusters	95.8 ± 1.0
Charge identification	93.2 ± 1.5
Total efficiency	35.8 ± 1.5

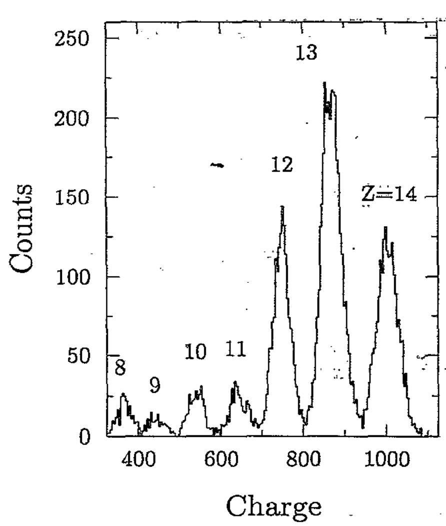

FIG. 2. Charge measurement for the selection of $Z = 13$ heavy ions for $1p$ triggered events. The charge of the heavy ions was measured in the downstream Si detector and the vertical and horizontal forward scintillators. The data shown here are an average of the three measurements. Scintillation counters pulse heights are corrected for saturation effects and the normalization is chosen to place $Z = 14$ particles at channel 1000.

The above criteria are used to identify events for the cross-section measurements. At this stage of the analysis, no information from the tracking chambers is required, and therefore the efficiency of these chambers does not enter in the determination of the cross sections. The efficiency for the selection criteria, shown in Table I, is measured using an unbiased (pretrigger) data sample. We estimate a systematic uncertainty of 5% for the cross sections.

IV. EVENT RECONSTRUCTION

We reconstruct the tracks in the forward spectrometer by performing a crude pattern recognition, followed by a detailed fitting of the tracks, successively combining information from the detectors to perform more tightly constrained fits. The steps are as follows.

(1) Pattern recognition is carried out by the establishment of "roads" based on pulse heights measured in the forward scintillators and the cathode pad sections of DC2 and DC3. Such roads are defined to an accuracy of

the width of the pad sections, which vary over the plane (6.4 to 12.7 mm in DC2 and 12.7 to 25.4 mm in DC3). The road is extrapolated through the magnet to the target, and hits in DC1, DC2, and DC3 (drift and pad sections) which are consistent with the roads are identified and, along with the hits in the beam vertex detector, are passed on to our track reconstruction program.

(2) In the track reconstruction stage, consistent hits within DC2 or DC3 are identified by first demanding that the sum of drift times for charge clusters drifting in opposite directions fall within a window corresponding to ± 1.0 mm in space. Centroids of pairs of hits satisfying this criterion are then formed, and principal component analysis [13] is used to locate the set of drift chamber hits which are most consistent with a straight line segment falling within the road. The use of such centroids eliminates the left-right ambiguities.

(3) Using the hits identified in the preceding step, a fit is performed to the measured drift time values in DC2 and DC3, the horizontal and vertical positions identified in DC1, and the vertical positions found in the the cathode pad sections of DC2 and DC3. Because of the inaccuracy of the vertical measurements, the track is constrained to pass through $y = 0$ at the target. The vertical distribution of the beam particles is approximately Gaussian, centered at $y = 0$ with FWHM ≈ 6 mm. Because the trajectory passes through the magnet, the value of rigidity for the track is introduced as a variable in this fit, along with the horizontal and vertical slopes and intercepts of the tracks at the position of the target.

(4) A geometrically constrained fit is performed, in which the horizontal position of the beam track, found from the upstream silicon strip detectors, intersects with the horizontal positions of the two downstream tracks, which are required to have the same vertical coordinate at the target. This fit imposes three geometrical constraints.

(5) A kinematically constrained fit is performed, in which it is assumed that the decaying Si nucleus has the same velocity as the beam track, but whose invariant mass is increased by the final-state energy, which is introduced as a variable in the fit. Two center-of-mass decay angles (θ^* and ϕ^*) are also introduced as variables, along with the horizontal and vertical slopes and intercepts of the incoming track. Here θ^* is defined as the polar angle of the ^{27}Al momentum vector with respect to the beam momentum vector in the rest frame of the projectile (because of our assumption that the velocity of the projectile is unchanged in the EMD process, this is also the rest frame of the excited state), and ϕ^* is the azimuthal angle of the decay plane about the beam momentum vector, referred to the horizontal plane. In this fit, the masses of the final-state particles [14] are assumed, and momentum conservation is imposed. We also introduce at this point parameters to account for multiple scattering in the horizontal plane for both the proton and heavy ion tracks in the three regions where significant amounts of material are concentrated: the target, DC1, and DC2. The technique used is the "optimum track fitting" method described by Lutz [18], in which the "observed" value scattering angle is zero and the error in the observation is the calculated rms value of the scattering angle projected onto a plane. Since each parameter is accompanied by an observation, this method introduces no change in the number of degrees of freedom in the fit. The kinematic fit imposes two additional constraints beyond those required by the geometric fit.

We reconstruct about 75% of the events selected for the cross-section analysis. The major loss arises from demanding that there is one and only one hit in each counter of the beam vertex detector. We lose 15% of the events due to this criterion because of dead or noisy strips in the detectors. In 5% of the events, we fail to locate a sufficient number of hits in either DC2 or DC3 within the roads established by the pad sections of these chambers (there is a loss of the proton hit in DC1 due to its proximity to the heavy ion track in 20% of the cases, but this does not prevent us from reconstructing the event). Finally, 5% of the events fail at the reconstruction stage, due to lack of convergence of either the geometric or kinematic fit. The loss arising from the beam vertex detector simply excludes certain values of the beam angle and position. The remaining losses are quite small and are not obviously related to any particular event topology. Because the distributions of geometrical and kinematic quantities closely resemble those obtained in our simulation, we believe that any biases due to reconstruction inefficiencies are negligible.

The E814 tracking chambers [11, 12] were designed to detect minimum ionizing particles as well as heavy fragments. The peripheral interactions producing $p+^{27}$Al require good performances of both types of particles with high precision. Our pattern recognition method (described above) indicates that the horizontal spatial resolution in each drift chamber plane for both tracks is

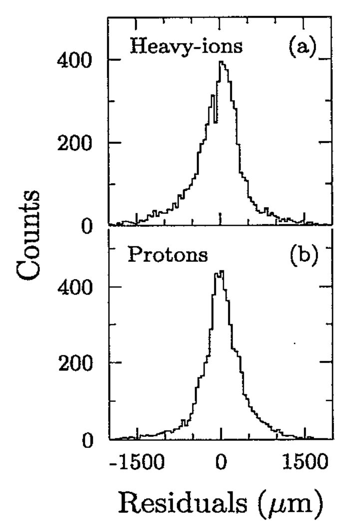

FIG. 3. Distribution of residuals in one plane of DC2 for reconstructed (a) heavy ion ($\sigma = 320$ μm) and (b) proton tracks ($\sigma = 305$ μm). Only hits that pass through the selection criteria on the sum of drift times in neighboring planes, discussed in the text, are included. The widths of these curves are used to establish values for the position uncertainty in the track reconstruction.

TABLE II. Reconstructed invariant mass and decay angular resolutions. These values have been obtained from our Monte Carlo simulation, which contains the effects of detector resolution and multiple Coulomb scattering.

Source of uncertainty	σ_M (MeV)	σ_{θ^*} (deg)	σ_{ϕ^*} (deg)
Detector resolution	0.5	1.0	2.5
Multiple scattering with no target	0.2	0.5	0.8
Total for Al target	0.6	1.3	3.2
Total for Cu target	0.7	1.6	4.0
Total for Sn target	1.0	2.1	5.0
Total for Pb target	1.1	2.6	6.0

approximately 300 μm, even though the heavy ion tends to produce more δ rays than the proton. Figures 3(a) and 3(b) show the residuals obtained for ^{27}Al tracks and proton tracks in DC2, respectively. In DC3 a position resolution similar to that for DC2 was achieved.

The kinematic reconstruction code is tested by means of simulating, for known kinematic conditions, the positions of the tracks in all the detection planes of the experimental apparatus, and reconstructing them. This procedure also serves to study the contributions of the various factors affecting the resolution of the reconstructed quantities, which arise from position distortions caused by the detector resolution and by multiple scattering in the air or otherwise not accounted for by the optimum track fitting method. The results of these studies are shown in Table II. The simulation code also permits an estimate of the systematic errors in the final-state energy scale arising from uncertainty in the beam momentum, the field strength and effective length of the spectrometer magnets, and detector alignments. We estimate this systematic error to be less than 0.5 MeV.

V. RESULTS

To characterize the nature of the reaction mechanism we investigate the production cross section as a function of the target. As mentioned in Sec. III, the principal background to this process comes from soft nuclear-induced fragmentation. The probability for these collisions depends on the target size, whereas the probability for EMD depends on the target charge. Figure 4 shows the measured single proton emission cross sections as a function of target charge for five different targets. These data are corrected for interactions outside of the target by subtracting the appropriately scaled rates of events observed with the empty target frame. Errors on the data are somewhat larger than those given by Poisson statistics, as they are derived from the observed dispersion of our measurements from different runs for the same target. The cross sections exhibit strong charge dependence but not a simple Z_T scaling. To obtain the dependence of the EMD cross sections with Z, we fit the data assuming the following dependence of the cross section, leaving a, b, and c as free parameters:

$$\sigma = a({A_T}^{1/3} + {A_P}^{1/3}) + bZ^c .$$

In the above equation A_T, A_P, and Z are the target mass, projectile mass, and target charge, respectively. The first term, which scales as the sum of the radii of the target and projectile nuclei, is expected to describe the target dependence of the nuclear component, whereas the second term, which scales as a power of the target charge, is expected to describe the target dependence of the electromagnetic component. The values of the parameters obtained from the fit are $a = 1.34 \pm 0.19$, $b = 0.23 \pm 0.05$, and $c = 1.80 \pm 0.06$. The contribution of each term to the cross section is shown in Fig. 4. The results indicate a non-negligible contribution from nuclear processes for low-Z targets. However, our value of a cannot be taken as a measurement of the nuclear component of the cross section, due to the severe biases introduced by the trigger and the analysis. The observed $Z^{1.8}$ dependence of the electromagnetic component is in agreement with values observed in other EMD studies [8]. Even though for low-Z targets the nuclear component is substantial,

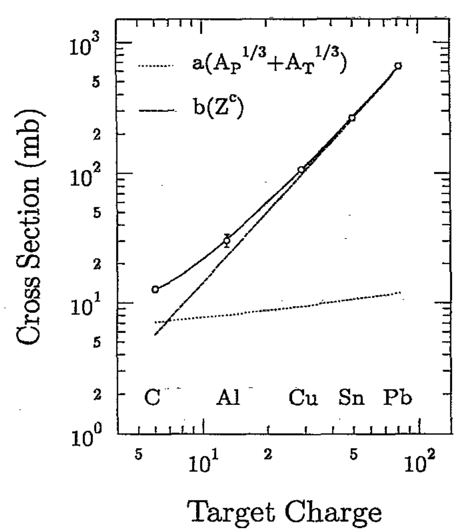

FIG. 4. Cross section for ^{28}Si $\rightarrow 1p+^{27}$Al for the five targets used in this experiment. The fit, discussed in the text, is a simple two-component model, with one term, the nuclear component (dotted line), proportional to $(A_T^{1/3} + A_P^{1/3})$, and the other, the electromagnetic component (dashed line), proportional to Z_T^c. The solid line is the sum of the two.

the background to EMD for high-Z targets is negligible, which opens the possibility for meaningful detailed studies using kinematic reconstruction.

Events used in the evaluation of the cross sections are processed as described in the previous sections to generate final-state energy distributions and decay angular distributions in both θ^* and ϕ^*. The raw final-state energy distributions for the selected events produced on Pb, Sn, Cu, and Al targets are shown in Fig. 5. These data have also been corrected for interactions outside the target, as described above. Empty target subtraction results in a correction of $\sim 5\%$ in Pb to $\sim 30\%$ in Al. The rapid rise of the data near threshold confirms our estimates of the experimental resolution in the invariant mass shown in Table II. All the distributions show a similar peak centered at about 18 MeV with a relatively narrow width of about 7 MeV. These values can be compared with the peak position (20 MeV) and width (4.5 MeV) of the giant dipole resonance in ^{28}Si as determined in the (γ, p) reaction [15, 16]. It should be noted that in the electromagnetic excitation process, the virtual photon spectrum is not uniform and tends to excite the low end of the GDR distribution preferentially. The decay to excited states in the ^{27}Al also tends to skew the distribution to the low side.

The center-of-mass angles for this process are obtained from the kinematic reconstruction, and the measured θ^* and ϕ^* distributions are presented in Fig. 6. Within statistics both distributions are symmetrical and very nearly isotropic. The observed symmetry gives confidence in the event reconstruction. A detailed theoretical calculation of the angular distribution is complicated because decays proceed to several excited states of the residual nucleus. It should be noted that the preference for emission perpendicular to the beam axis suggested by Bertulani and Baur [7] is not observed.

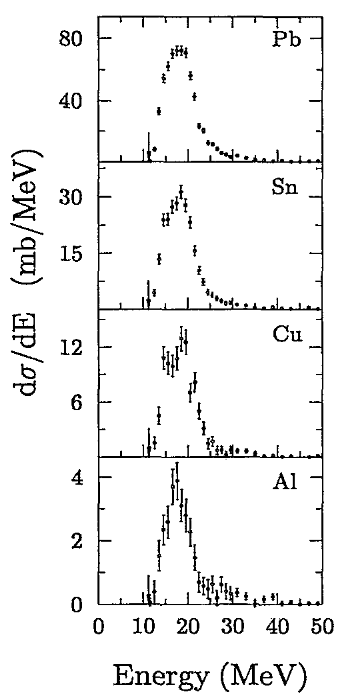

FIG. 5. Raw ^{28}Si final-state energy distribution for four targets used in the experiment. Contributions to the data arising from interactions outside the target have been subtracted, using data taken with the empty target frame. The arrows indicates the kinematic threshold.

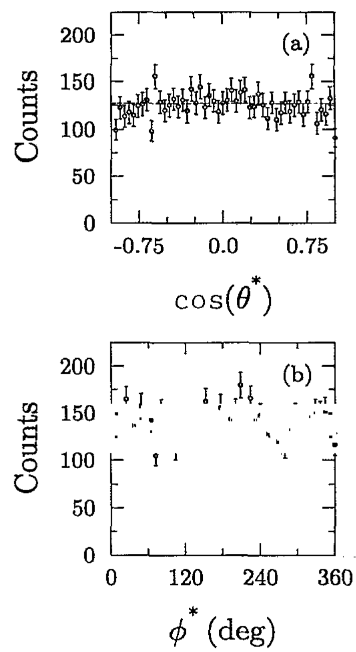

FIG. 6. Decay angular distributions for reconstructed events taken with Pb target. The angles are the (a) polar (θ^*) and (b) azimuthal (ϕ^*) center-of-mass angles of the ^{27}Al ion. The points are consistent with angular isotropy as is indicated by the lines drawn at the mean of the distributions.

Under the assumption that the process is factorizable, i.e., that the differential cross section is proportional to $N_\gamma \sigma(\gamma, p)$, where N_γ is related to the excitation mechanism, ratios of the energy spectra for different targets can provide some insight into the dependence of the reaction mechanism as a function of the excitation energy. For example, if the excitation is purely electromagnetic, the ratios should scale with target charge as a power of Z, and, in fact, should be equal to the ratios of the calculated photon spectra for the two targets. On the other hand purely nuclear excitation should give a ratio proportional to the sum of the target and projectile radii. In Figs. 7(a) and 7(b) are shown the experimental ratios for Pb/Sn and Pb/Al compared with the values expected from the two terms EMD and nuclear (dotted lines) extracted from the fit performed on the integrated cross sections. In addition, we show the curve which is the ratio of the calculated photon spectra (dashed lines) for the two targets. In the calculation of the photon spectra, it is assumed that the minimum impact parameter $b_{\min}$ is the sum of the target and the projectile radii:

$$b_{\min} = 1.2(A_T^{1/3} + A_P^{1/3}).$$

For the Sn target, the ratios near the GDR are fairly consistent with the calculated ratio. This is not the case for Al, where the experimental ratios are much lower

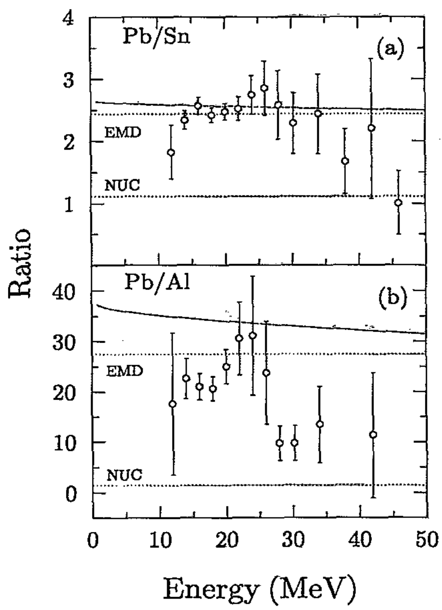

FIG. 7. Ratio of final-state energy spectra for different targets: (a) Pb/Sn ratio and (b) Pb/Al ratio. The dotted lines indicate the excitation energy-independent levels of the EMD and nuclear components found from our fit to the total cross sections. The dashed curve is the ratio of the calculated virtual photon spectra, using the WW approximation. Points near the lower dotted line, especially evident in the Pb/Al ratio, indicate the presence of significant nuclear-induced background.

than the calculated values. The nuclear background is clearly the dominant process at the high end of the energy spectrum ($E > 25$ MeV). The data also indicate some background at low final-state energies. The ratios of the calculated WW spectrum are consistently higher than the data, but, as indicated in Fig. 7, a simple $Z^{1.8}$ scaling of the photon spectrum fits the data quite well, at least in the vicinity of the GDR.

In order to evaluate the contribution of the nuclear-induced background as a function of final-state energy, we use a technique similar to that used for the integrated cross sections in which we exploit our knowledge of the expected scaling with target mass and charge. Such an approach is required, since the two processes lead to the same final state and they are not distinguishable on an event-by-event basis. We proceed by obtaining an approximate experimental distribution for the nuclear component by assuming that the data from the Pb target has very little nuclear background. In order to obtain sufficient statistical accuracy, we first rebin the data in Fig. 5 into the energy bins of widths 2–4 MeV (see Table III). We scale the Pb data by the factor $(Z_{\rm C}/Z_{\rm Pb})^{1.8}$ and subtract it from the data taken with the carbon target (not shown in Fig. 5), yielding the distribution for the nuclear induced component as shown in Fig. 8. We find that a suitable parametrization for this distribution is a sum of a Gaussian and Moyal function, each with three free parameters.The function used is

$$f_{\rm nuc} = X_1 e^{-\mu^2/2} + X_2 e^{-(\lambda+e^{-\lambda})/2}$$

in which $\mu = (E - X_3)/X_4$ and $\lambda = (E - X_5)/X_6$.

Our procedure is to perform a fit of the following function to the entire data set:

$$d\sigma_k/dE = (A_T^{1/3} + A_P^{1/3}) f_{\rm nuc} + Z^{1.8} C_k(E_k)$$

in which the six nuclear parameters (X_i) and 14 values of C_k (one for each value of the final-state energy E_k) are varied to minimize the χ^2 for the fit.

In order to test the method of separating the two components, we first perform a fit to the data from the four targets Pb, Sn, Cu, and Al, and use the result to predict the nuclear component for the C data. In order to achieve sufficient accuracy for this test, it is necessary to also represent C_k as a parameterized function (for this we use the same form as we use for $f_{\rm nuc}$, which we find adequately represent the data). The comparison is shown as the dashed curve in Fig. 8. We emphasize that in this fit no data from the carbon target was used. The function $f_{\rm nuc}$ found in this fit is clearly consistent with the nuclear component of the carbon data and demonstrates the validity of the method. In order to achieve the highest possible accuracy for this subtraction, the C data are included in the final fit. The nuclear component resulting from this fit is shown as the solid line in Fig. 8. The χ^2 found for this fit is 31.6 for 50 degrees of freedom. Finally, we subtract the fitted nuclear component from each of the data points of Fig. 5, yielding experimental EMD cross sections for each target. The

TABLE III. Values of the cross-section parameters $C_k = (1/Z^{1.8}) d\sigma_{\rm EMD}/dE$ found in the final fit to the data taken with Pb, Sn, Cu, Al, and C targets. These parameters represent, at each value of the final-state energy, the target-averaged values for the EMD component of the cross section, divided by $Z^{1.8}$.

E_k (MeV)	C_k (μb/MeV)	E_k (MeV)	C_k (μb/MeV)
11–13	1.48 ± 0.19	25–27	3.24 ± 0.22
13–15	15.62 ± 0.49	27–29	1.63 ± 0.17
15–17	22.55 ± 0.59	29–32	1.12 ± 0.13
17–19	25.31 ± 0.62	32–36	0.54 ± 0.08
19–21	22.24 ± 0.56	36–40	0.30 ± 0.06
21–23	11.81 ± 0.39	40–44	0.17 ± 0.05
23–25	5.56 ± 0.28	44–48	0.09 ± 0.03

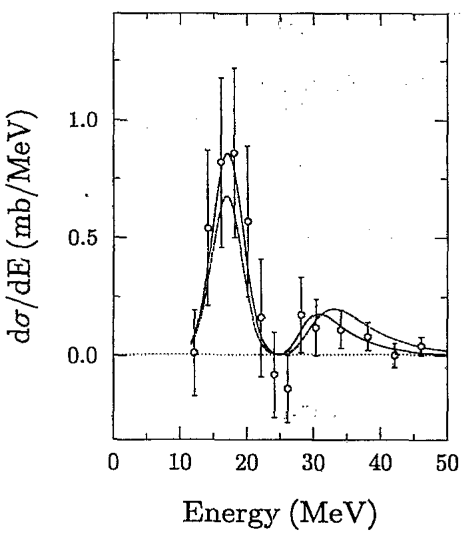

FIG. 8. Estimated cross-section distribution of the surviving nuclear-induced component of the cross section for the C target, obtained by subtracting the raw Pb data, scaled by the factor $(Z_C/Z_{Pb})^{1.8}$, from the C data. The dashed curve represents the evaluation of the nuclear component using Z and A scaling (described in the text) in a fit to the data from the Pb, Sn, Cu, and Al targets. The solid curve is the result of a similar fit to all five targets, and this function, when appropriately scaled with the target mass, is subtracted from the data of Fig. 5 to give the EMD component shown in Fig. 9.

background-subtracted EMD final-state energy spectra are shown in Fig. 10 for the Pb, Sn, Cu, and Al targets. As expected, the effects of nuclear excitation are negligible for the heavier targets. For the Al target, the main effect is to reduce the cross section at the peak by approximately 20% and to reduce significantly the high energy tail. In Table III we give the results of the EMD component resulting from the fit, which represents an average over the data from all the targets. The fit also yields values for the nuclear component, but it cannot be viewed as a meaningful measurement of the nuclear-induced component of the cross section, since the trigger and the event selection procedure introduce severe biases for this process.

We now compare the results of this experiment to data on the photonuclear process. To do so, we use the available data on the $^{28}Si(\gamma,p)^{27}Al$ reaction [15, 16] and combine it with a WW photon spectrum to predict the results expected in our experiment. The simulation program assumes that the excitation proceeds through virtual photons with a WW spectrum. It uses experimental (γ,p) cross sections for ^{28}Si measured up to $E_\gamma = 26.0$ MeV, and takes into account the decay to excited states of ^{27}Al up to an energy of 4.5 MeV [15], as follows. The (γ,p) cross sections as a function of E_γ for each state in ^{27}Al are first multiplied by the virtual photon spectrum to obtain effective final-state yields as a function of photon energy. The values of these yields, integrated over photon energy, are used to obtain effective branching ratios for each state. Monte Carlo techniques are employed to first choose the excited state based on these effective branching ratios, and to then generate a value of E_γ according to the strength distribution of the state being considered. In the case of decay to an excited state of ^{27}Al, the energy of the proton is reduced, skewing the observed final-state energy distribution to the lower end, as mentioned above. The decay is assumed to be isotropic. Effects of multiple scattering and detector resolution are included in the simulation.

We measure the invariant mass or final-state energy of the $p+^{27}Al$ system; however, the quantity of physical interest is the excitation energy, which is the sum of the final-state energy and the energy of any undetected decay photons from the ^{27}Al nucleus. The simulation code permits a study of the relationship between the two. In Fig. 9 we show the expected final-state energy distribution for the calculation described above, which utilizes the effective branching ratios obtained from photonuclear data. For comparison we also show the excitation energy distribution, obtained by adding the energy of the decay photon to the final-state energy. We take the difference between the two curves as an estimate of the systematic uncertainty made in interpreting the final-state energy as the excitation energy. Note that in the simulation, we have included only excited states of ^{27}Al of 4.5 MeV or lower. The existence of higher excited states will affect the difference between the excitation energy and final-state energy; however, for values of ^{28}Si excitation energy below 20 MeV, it is unlikely that states of energy above 4.5 MeV will be excited, considering the proton separation energy and the Coulomb barrier.

The final-state energy curves obtained from the Monte Carlo simulation are displayed for comparison with the

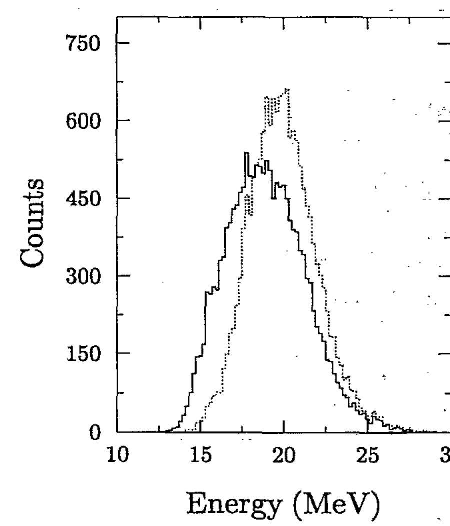

FIG. 9. Monte Carlo simulation of the final-state energy distribution (solid curve) and the excitation energy distribution (dashed curve), obtained by adding the energy of the decay photon to the final-state energy. The calculation is for a Pb target. The curves were obtained by combining the virtual photon spectrum in the WW approximation with cross sections and effective branching ratios for the photonuclear $^{28}Si(\gamma,p)^{27}Al$ process. Effects of experimental resolution and multiple Coulomb scattering are included in the calculation.

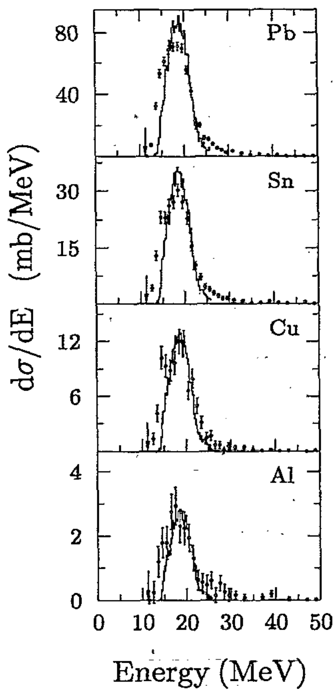

FIG. 10. Nuclear-subtracted final-state energy distributions for reconstructed events taken with Pb, Sn, Cu, and Al targets. The solid curves are obtained from (γ, p) experimental data multiplied by the virtual photon spectrum and simulated through our apparatus. Normalization of the simulated data is based solely on the experimental photoabsorption cross sections. The arrows indicate the kinematic threshold. The resolution in final-state energy, given as σ_M in Table II, is approximately 1 MeV or less and is target dependent. See text for a discussion of the relationship between final-state energy and the excitation energy.

data in Fig. 10. There are no adjustable parameters in this comparison. Since the simulation uses $\sigma(\gamma, p)$ cross-section data only in the interval 15.4–26.0 MeV, a comparison beyond 26.0 MeV cannot be made. The simulated cross sections, integrated over the excitation energy, over the interval 16.0–26.0 MeV, agree well with the data, as is shown in Table IV. However, there is a small discrepancy in shape which appears at the low end of the spectrum. We have attempted to understand whether the discrepancy in shape is due to instrumental effects by simulating the events under different conditions of detector alignment and resolution. Although noticable differences in the decay angular distributions can be produced, the final-state energy spectrum is insensitive to such changes. The observed discrepancy could be an indication of the inability to explain the excitation of the resonance with a simple WW approximation or the effect of excited states of ^{27}Al above 4.5 MeV, as mentioned above.

TABLE IV. Integrated cross sections in the interval 16.0 to 26.0 MeV. The errors for the simulation are deduced from the available $^{28}\mathrm{Si}(\gamma, p)^{27}\mathrm{Al}$ photoabsoption cross sections which are used as the input. Errors on the data are statistical, with appropriate corrections for the effects of empty target subtraction and the separation of EMD and nuclear components as discussed in the text. In addition, the cross-section scale is uncertain by 5%.

Target	Data (mb)	Simulation (mb)
Al	19.5 ± 1.5	15 ± 4
Cu	88.0 ± 3.6	72 ± 20
Sn	221.5 ± 4.7	203 ± 55
Pb	559.7 ± 8.0	515 ± 141

VI. CONCLUSIONS

We have presented measurements of final-state energy distributions and cross sections, along with the angular distributions for the decay products for the electromagnetic dissociation of ^{28}Si. The cross sections are in good agreement with those measured previously [1]. Because the two experiments differ considerably, particularly in the detectors used to veto nuclear events, the agreement of the two results indicate that the event selection procedure and efficiency estimates are sound.

The soft nuclear-induced background to the EMD in the final-state energy distributions was evaluated by representing this component with a simple functional form, whose parameters were determined by a fit to the data for all targets. The resulting EMD spectrum was compared to the results of a simulation based on a folding of the WW virtual photon spectrum produced by the targets with the inverse photonuclear process $^{28}\mathrm{Si}(\gamma, p)^{27}\mathrm{Al}$. In general, the agreement is satisfactory, but some discrepancy is observed at low final-state energy. A similar effect has been seen in the data on the EMD of ^{16}O at lower beam energy [17].

The present paper has shown that at relativistic energies it is possible to measure the properties of excited heavy ion projectiles with resolution good enough to probe their structure. For example, resolution in the invariant mass of 0.6–1.1 MeV, depending on the target, has been attained. Center-of-mass angles were reconstructed to an accuracy of a few degrees. The resolution in both energy and angle is dominated by the multiple scattering in the target. The technique shown here can be applied to other nuclei and decay channels as well. It could be used for example to explore the collective states in the continuum of unstable nuclei or to explore the existence of collective strength at high excitation energy, above the GDR. In addition, correlation studies of final states containing identical nucleons are possible using precision kinematic reconstruction of exclusive channels.

We acknowledge the excellent support by the BNL AGS and Tandem staffs and Dr. H. Brown for expert help in the design and running of our beam line. This research is supported, in part, by the U.S. Department of Energy, the National Science Foundation, the Natural Sciences and Engineering Research Council of Canada, and the Conselho Nacional de Pesquisa e Desenvolvimento (CNPq).

[1] J. Barrette, P. Braun-Munzinger, W.E. Cleland, G. David, E. Duek, M. Fatyga, D. Fox, S.V. Greene, J.R. Hall, R. Heifetz, T.K. Hemmick, N. Herrmann, R.W. Hogue, G. Ingold, K. Jayananda, D. Kraus, A. Legault, D. Lissauer, W.J. Llope, T. Ludlam, R. Majka, D. Makowiecki, S.K. Mark, J.T. Mitchell, M. Muthuswamy, E. O'Brien, L.H. Olsen, V. Polychronakos, M. Rawool-Sullivan, F.S. Rotondo, J. Sandweiss, B. ShivaKumar, J. Simon, U. Sonnadara, J. Stachel, J. Sunier, H. Takai, T.G. Throwe, H. VanHecke, L. Waters, W.J. Willis, K. Wolf, D. Wolfe and C.L. Woody, Phys. Rev. C **41**, 1512 (1990).

[2] T. Kobayashi, S. Shimoura, I. Tanihata, K. Katori, K. Matsuta, T. Minamisono, K. Sugimoto, W. Müller, D.L. Olson, T.J.M. Symons, and H. Wieman, Phys. Lett. B **232**, 51 (1989).

[3] D.L. Olson, B.L. Berman, D.E. Greiner, H.H. Heckerman, P.J. Lindstron, G.D. Westfall, and H.J. Crawford, Phys. Rev. C **24**, 1529 (1981).

[4] J.C. Hill, F.K. Wohn, J.A. Winger, M. Khayat, and M.T. Mercier, Phys. Rev. C **39**, 524 (1989).

[5] C. Brechtmann and W. Heinrich, Z. Phys. A **331**, 463 (1988).

[6] J.D. Jackson, *Classical Electrodynamics* (Wiley, New York, 1975).

[7] C. Bertulani and G. Baur, Phys. Rep. **163**, 299 (1988).

[8] D. Lissauer and H. Takai, Phys. Rev. C **41**, 2410 (1990).

[9] C. Brechtmann, W. Heinrich, and E.V. Benton, Phys. Rev. C **39**, 2222 (1989).

[10] W.J. Llope and P. Braun-Munzinger, Phys. Rev. C **41**, 2644 (1990).

[11] J. Fischer, D. Lissauer, T. Ludlam, D. Makowiecki, E. O'Brien, V. Radeka, S. Rescia, L. Rogers, G.C. Smith, D. Stephani, B. Yu, S.V. Greene, T.K. Hemmick, J.T. Mitchell, and B. Shivakumar, IEEE Trans. Nucl. Sci. NS-**37**, 82 (1990).

[12] R. Debbe, J. Fischer, D. Lissauer, T. Ludlam, D. Makowiecki, E. O'Brien, V. Radeka, S. Rescia, L. Rogers, G.C. Smith, D. Stephani, B. Yu, S.V. Greene, T.K. Hemmick, J.T. Mitchell, and B. Shivakumar, IEEE Trans. Nucl. Sci. NS-**37**, 88 (1990).

[13] H. Wind, in *Formulae and Methods in Experimental Data Evaluation* (European Physical Society, 1984), Vol. 3, Chap. K.

[14] A.H. Wapstra and K. Bos, At. Data Nucl. Data Tables **19**, 177 (1977).

[15] R.L. Gulbranson, L.S. Cardman, A. Doron, A. Erell, K.R. Lindgren, and A.I. Yavin, Phys. Rev. C **27**, 470 (1983).

[16] E. Kerkhove, P. Berkvens, R. Van de Vyver, H. Fardinande, P. Van Otten, D. Ryckbosch, and E. Van Camp, Nucl. Phys. **A474**, 397 (1987).

[17] D.L. Olson, M. Baumgatner, D.E. Greiner, P.J. Lindstrom, T.J.M. Symons, R. Wada, M.L. Webb, B.L. Berman, H.J. Crawford, and J.M. Engelage, Phys. Rev. C **44**, 1862 (1991).

[18] G. Lutz, Nucl. Instrum. Methods, Phys. Res. A **273**, 349 (1988).